ACADEMIC PRESS

Numerical simulation of the winter polar wave clouds observed by Mars Global Surveyor Mars Orbiter Laser Altimeter

G. Tobie,* F. Forget, and F. Lott

Laboratoire de Météorologie Dynamique (LMD), Université Pierre et Marie Curie, Tour 25-15, 5ème étage, 4, place Jussieu, 75252 Paris cedex 05, France

Abstract

In 1998, the Mars Orbiter Laser Altimeter revealed the presence of isolated or quasi-periodic thick clouds during the martian polar night. They are believed to be composed of CO_2 ice particles and to be tilted against the wind direction, a feature characteristic of vertically propagating orographic gravity waves. To support that interpretation, we present here numerical simulations with a two-dimensional anelastic model of stratified shear flow that includes simple CO_2 ice microphysics. In some of the simulations presented, the orography is an idealized trough, with dimensions characteristic of the many troughs that shape the Mars polar cap. In others, it is near the real orography. In the polar night conditions, our model shows that gravity waves over the north polar cap are strong enough to induce adiabatic cooling below the CO_2 frost point. From this cooling, airborne heterogeneous nucleation of CO_2 ice particles occurs from the ground up to the altitude of the polar thermal inversion. Although the model predicts that clouds can be present above 15 km, only low altitude clouds can backscatter the Laser beams of MOLA at a detectable level. Accordingly, the shape of the Laser echoes is related to the shape of the clouds at low level, but do not necessarily coincide with the top of the clouds. The model helps to interpret the cloud patterns observed by MOLA. Above an isolated orographic trough, an isolated extended sloping cloud tilted against the wind is obtained. The model shows that the observed quasi-periodic clouds are due to the succession of small-scale topographic features, rather than to the presence of resonant trapped lee waves. Indeed, the CO_2 condensation greatly damps the buoyancy force, essential for the maintenance of gravity waves far from their sources. Simulations with realistic topography profiles show the cloud response is sensitive to the wind direction. When the wind is directed upslope of the polar cap, on the one hand, a large scale cloud, modulated by small-scale waves, forms just above the ground. On the other hand, when the wind is directed downslope, air is globally warmed, and periodic ice clouds induced by small-scale orography form at altitudes higher than 3–5 km above the ground. In both cases, a good agreement between the simulated echoes and the observed one is obtained. According to our model, we conclude that the observed clouds are quasi-stationary clouds made of moving ice particles that successively grow and sublimate by crossing cold and warm phases of orographic gravity waves generated by the successive polar troughs. We also find that the rate of ice precipitation is relatively weak, except when there is a large scale air dynamical cooling.

Keywords: Mars, atmosphere; Atmosphere, dynamics; Clouds; CO_2 ices

1. Introduction

Since 1998, the Mars Orbiter Laser Altimeter (MOLA) aboard the Mars Global Surveyor (MGS) orbiter has observed optically thick clouds above the winter north and south polar caps (Zuber et al., 1998; Smith et al., 2001a). The fact that they are only present during the winter polar night suggests that they are constituted of CO_2 ice parti-

cles (Ivanov and Muhleman, 2001). These clouds are detected from the surface up to altitudes of 15–20 km above the ground. Some of them are isolated while others present quasi-periodic successive patterns. Typical isolated clouds are found to be extended from the surface to altitudes of 4–6 km above the surface (Pettengill and Ford, 2000). Whatever their shape and their vertical extension are, they all look tilted against the dominant wind, with a slope between zero to twenty degrees (Ivanov and Muhleman, 2001).

These observations suggest that they are produced by mountain waves and that their periodic patterns might be due to the presence of trapped lee waves (Pettengill and Ford, 2000; Zuber et al., 1998). The fact that these clouds are trig-

* Corresponding author. Present address: Laboratoire de Planétologie et Géodynamique, UFR des Sciences et Techniques, 2, rue de la Houssinière, BP 92208, 44322 Nantes cedex 03, France.
    E-mail address: tobie@chimie.univ-nantes.fr (G. Tobie).

gered by the orography is further supported by the fact that the topography on Mars presents large mesoscale irregularities near the poles. For instance, the north polar ice cap is elevated above its surrounding with a 3 km maximum elevation near the pole (Zuber et al., 1998). It is sculpted by spiral troughs, whose typical depth and half-depth width are around 0.5 and 7 km (Ivanov, 2000), respectively.

For the last thirty years, CO_2 ice clouds attributed to mountain waves have been observed in the lee of craters or large volcanoes (Hunt and Pickersgill, 1984). Before 1998, clouds have never been directly observed above the winter polar caps, although their presence during the polar night had been intuited for a long time (Gierash and Goody, 1968; Pollack et al., 1990; Forget et al., 1995). Indeed, the clouds optical properties can explain the low brightness temperature areas observed on the winter polar cap (Kieffer et al., 1977; Forget et al., 1995). They can also play a key role in the martian climate, which greatly depends on the condensation of CO_2 in polar night conditions (Yokohata et al., 2002). Accordingly, these clouds may need to be parameterized in General Circulation Models, and a better understanding of their life cycles is essential for this purpose.

Following the Mariner 9 and Viking observations, dynamical models have been proposed to explain the formation of clouds by lee waves (Pirraglia, 1976; Pickersgill and Hunt, 1979). These studies did not investigate (i) the occurrence of lee waves when the atmosphere is near the frost point, and (ii) the dynamical coupling between CO_2 ice condensation and the wave dynamics. The first objective of this paper is to address these two issues. The second objective is to give further evidence that the organized structures, seen in the MOLA echoes, are produced by CO_2 ice clouds triggered by orographic gravity waves. For these purposes, we have developed a model that couples 2D stratified flow dynamics with CO_2 ice cloud physics. The dynamical model solves the anelastic equations of motion (Lipps and Hemler, 1991), and has been used for the Earth atmosphere to study mountain waves (Lott, 1998; Georgelin and Lott, 2001). The cloud model includes simple CO_2 ice microphysics, sedimentation and wind advection. In all the simulations presented, the background flow is representative of the martian winter north polar cap climatology. It is consistent with the climatologies of the LMD martian GCM (Forget et al., 1999) and the available MGS observations.

To address the relative importance of the dynamical and physical processes responsible of the existence of these clouds, the simulations done are presented in order of increasing complexity. In Section 2, we examine the generation of gravity waves by a single orographic trough in a noncondensing north polar winter atmosphere as well as the impact of the release of latent heat due to CO_2 condensation. We examine to which extent the regular structure can be related to resonant trapped waves, and to which extent their dynamics is affected by the CO_2 ice condensation. These simulations serve as a basis to interpret the more realistic ones, presented in Section 4. In Section 3, we give a description of CO_2 ice cloud physics and the basis driving wave cloud formation. Numerical simulations with these cloud physics and realistic north polar cap topographies are presented in Section 4. In order to compare with the MOLA cloud echo observation, we reconstruct from the model outputs the echoes the simulated clouds produce. In Section 5, we discuss these results and sum up the main points of our findings.

2. Dynamics of the mountain waves in the martian north polar night

2.1. The martian polar night atmosphere

The characteristic of the martian atmosphere within the polar night are quite unique. In the absence of solar energy, the temperature of the surface falls down to the condensation point of CO_2, leading to the formation of the dry ice seasonal polar caps. Above the surface, the radiative–convective processes also tend to cool the atmosphere to the frost point of CO_2. Therefore, in the major part of the polar night atmosphere, the temperature profile follows the condensation temperature profile. The corresponding thermal structure is very stable, with a typical lapse rate (-1 K km^{-1}) much less steep than the adiabatic lapse rate (-5 K km^{-1}). Such stable conditions are favorable to gravity waves that occur in stratified flows, as suggested by the high resolution thermal profiles recorded by the radio-occultation experiment of Mars Global Surveyor (Hinson, 2001). These profiles exhibit temperature oscillation with vertical wavelength of about 1 to 2 km and amplitude of the order of a few kelvins.

In some locations, the temperature of the polar night atmosphere can be significantly warmer than the frost point of CO_2 if the atmosphere is adiabatically warmed by the large-scale flow dynamics. On the one hand, this can happen near the surface when the wind blows downhill (foehn wind effect) as described in Forget et al. (1998) (conversely, ascending winds globally enhance the condensation). On the other hand, spacecraft observations (Jakosky and Martin, 1987; Smith et al., 2001b; Pearl et al., 2001) as well as modeling studies (Wilson, 1997; Forget et al., 1999) have shown that above 15 to 50 km, depending on the latitude, season, and dust loading, the atmosphere is always warmed by a descent of air forced by a convergence of mass above 50 km. This convergence results from a combination of a strong mean meridional circulation (Hadley cell) and wave (mostly tides) mean flow interaction (Forget et al., 1999; Wilson, 1997).

Another key parameter for the present study is the wind profile. No direct observations are available, but analysis of simulations performed with the LMD General Circulation Model suggest that the wind is near constant between a few tens of meters above the surface to at least 10 km, with a typical velocity of 10 m s^{-1}. On the one hand, this is due to the fact that the turbulent boundary layer is extremely thin, because of the high stability of the atmosphere. On the other

hand, in the free atmosphere, the wind does not strongly increase with altitude because the horizontal temperature gradient are small, the temperature being everywhere that of the condensation point. This is very different from what occurs at sunlit latitudes, where the wind increases with altitude to satisfy the thermal wind balance.

2.2. Waves in a noncondensing atmosphere

2.2.1. Theory

Gravity waves generated when a stratified air flow passes over a mountain have been extensively studied in the Earth atmosphere (Queney, 1947; see Smith, 1980, for a review). These waves are driven by the buoyancy force that acts on air parcels displaced vertically in a stably stratified environment. They are usually referred to lee waves because they are observed in the lee of mountains. Their intrinsic frequency is between the Brünt–Väisällä frequency,

$$N^2 = g \frac{\partial \theta_0}{\partial z} / \theta_0$$

(where g is the gravity, θ_0 is the background potential temperature) and the Coriolis frequency, $f = 2\Omega \cos \phi$ (where Ω is the rotation frequency of the planet and ϕ the latitude). In the 2D linear case, the response of the atmosphere to the mountain forcing can be analyzed in the Fourier space,

$$h(x) = \int_{-\infty}^{\infty} \hat{h}(k_x) e^{ik_x x} \, dk_x, \tag{1}$$

where $h(x)$ is the topography profile, $\hat{h}$ its Fourier transform and k_x the horizontal wavenumber associated with $\hat{h}$. The vertical propagation of each harmonic depends on the vertical structure of the incident flow, i.e., on its horizontal velocity $U_0(z)$ and potential temperature $\theta_0(z)$ profiles. Waves generated by a flow with uniform velocity $U_0 = cte$ and uniform stratification $N^2 = cte$, propagate freely upward along straight ray paths. When U_0 and N vary with altitude, the gravity waves are refracted and the shortest harmonics can be reflected at some altitudes and return to the ground where they are reflected again (Scorer, 1949). At these short wavelengths and through constructive or destructive interferences, only a finite number of modes can exist in the long term and downstream of the obstacle. They are often referred to as resonant trapped modes, because they correspond to the only disturbances that exist in the long term and in the absence of orographic forcing.

To study atmospheric lee waves, but excluding acoustic waves, the anelastic approximation is better adapted than the Boussinesq and hydrostatic approximations. In this approximation, freely propagating gravity waves and trapped mountain waves co-exist (the latter being excluded, for instance, in the hydrostatic approximation). In this framework, the two-dimensional $(x–z)$ equations of motion are (see, for instance, Scinocca and Shepherd, 1992):

$$\frac{d\vec{v}}{dt} + \vec{\nabla}(c_p \theta_0 \tilde{\pi}) + c_p \frac{d\pi_0}{dz} \tilde{\theta}_z = 0, \tag{2}$$

$$\vec{\nabla} \cdot (\rho_0 \vec{v}) = 0, \tag{3}$$

where $\vec{v}$ is the velocity field, c_p is the constant pressure heat capacity, ρ_0 the background density. In Eqs. (2) and (3), the Exner pressure, π, and the potential temperature, θ, have been written:

$$\pi = \left(\frac{p}{p_r}\right)^{\kappa} = \pi_0(z) + \tilde{\pi}(x, z, t), \tag{4}$$

$$\theta = T\pi^{-1} = \theta_0(z) + \tilde{\theta}(x, z, t), \tag{5}$$

where the zero subscript refers to the fluid at rest, the tildes represent perturbations, p_r is a constant reference pressure, $\kappa = R/c_p$, R is the gas constant and T the temperature. If we assume that the fluid at rest is in hydrostatic balance, and invoke the ideal gas law $p = \rho R T$, all the background thermodynamic fields are uniquely determined once $T_0(z)$ is specified. The continuity equation (3) allows to define the mass flux streamfunction ψ,

$$u = \frac{1}{\rho_0} \frac{\partial \psi}{\partial z}, \qquad w = -\frac{1}{\rho_0} \frac{\partial \psi}{\partial x}. \tag{6}$$

At the lower boundary, we impose that

$$w = U_0(0) \frac{\partial}{\partial x} h(x), \tag{7}$$

a linearization of the general free-slip boundary condition that is only valid when the nondimensional parameter $H_N = N(0)H/U(0) < 1$, where H is the maximum elevation (see for instance, Smith, 1980). When this condition is satisfied, the waves forced by the obstacle are well described by the linearized set:

$$\left(\frac{\partial}{\partial t} + U_0 \frac{\partial}{\partial x}\right)\omega' - \frac{d}{dz}\left(\frac{\Omega}{\rho_0}\right)\frac{\partial \psi'}{\partial x} - c_p \frac{d\pi_0}{dz} \frac{\partial \theta'}{\partial x} = 0, \tag{8}$$

$$\left(\frac{\partial}{\partial t} + U_0 \frac{\partial}{\partial x}\right)\theta' - \frac{N^2 \theta_0}{g\rho_0} \frac{\partial \psi'}{\partial x} = 0, \tag{9}$$

$$\psi'(0) = -\rho_0(0)U_0(0)h(x) \quad \text{at } z = 0, \tag{10}$$

where the primes replace the tildes in Eqs. (2) and (3) to indicate that only the linear part of the total disturbance is considered, and $\omega = \partial u/\partial z - \partial w/\partial x$ is the vorticity.

To describe the flow response, it is conventional to consider the steady limit. In this case, one particular harmonic forced at the ground,

$$\psi'(x, z) = \rho_0^{1/2} \text{Re}\left(\hat{\psi}(z) e^{ik_x x}\right), \tag{11}$$

has a vertical structure which is governed by the Taylor–Goldstein equation:

$$\frac{d^2\hat{\psi}}{dz^2} + \left(\frac{N^2}{U_0^2} - \frac{1}{U_0}\frac{d^2 U_0}{dz^2} - \frac{1}{\rho_0}\left(\frac{d\rho_0}{dz}\right)\frac{dU_0}{dz} \right.$$
$$\left. + \frac{1}{2\rho_0}\frac{d^2\rho_0}{dz^2} - \frac{3}{4\rho_0^2}\frac{d\rho_0^2}{dz} - k_x^2\right)\hat{\psi} = 0 \tag{12}$$

$$\Leftrightarrow \quad \frac{d^2\hat{\psi}}{dz^2} + \left(S(z) - k_x^2\right)\hat{\psi} = 0, \tag{13}$$

where $S(z)$ is the Scorer parameter (i.e., the index of wave refraction). For $S(z) - k_x^2 > 0$, the solution is of the form: $\hat{\psi} = Ae^{+ik_z z} + Be^{-ik_z z}$, and for $S(z) - k_x^2 < 0$, it is of the form: $\hat{\psi} = A'e^{+k_z z} + B'e^{-k_z z}$, where $k_z = \sqrt{(|S(z) - k_x^2|)}$. For the first case, there is vertical propagation, and for the second one, there is no vertical propagation and the harmonic is evanescent in the vertical direction. Because the Scorer parameter varies with altitude, there are circumstances where an harmonic propagates vertically at low level and becomes evanescent above a turning point Z_T with $S(Z_T) = k_x^2$ where they are reflected toward the ground. It is the basic mechanism driving the trapped modes mentioned before.

2.2.2. Background profiles and analysis of the Scorer parameter profiles

The main characteristics of the north polar winter lower atmosphere are that the temperature profile is usually near the CO_2 condensation temperature profile and that the wind profile is almost constant with altitude (see Section 2.1). In our analysis, the temperature is assumed to follow the CO_2 condensation temperature up to the polar thermal inversion altitude. We have assumed two profiles for the background wind conditions (Fig. 1a): a constant wind, U_0, and a more realistic one, U_1, that takes into account a wind gradient above 8 km. For the temperature, we have considered three different profiles (Fig. 1b): T_0 without thermal polar inversion, T_1 with a thermal inversion at $z = 15$ km, and T_2 with a thermal inversion at $z = 25$ km. These various background conditions yield to totally different Scorer parameter profiles (Fig. 1c). In all cases, only harmonics with horizontal wavelength larger than $2\pi/\sqrt{S(0)} = 6$ km can propagate upward at the ground. For (U_0, T_0), the Scorer parameter increases faintly with altitude, so there is no level where an harmonic that propagates vertically near the ground can become evanescent at some level above. For (U_1, T_1), harmonics with horizontal wavelengths between 6 km and $2\pi/\sqrt{S(50\,\text{km})} = 100$ km encounter a turning height between 10 and 50 km, and a large number of wavelengths are trapped at low altitude.

2.3. Dynamical model

The dynamical model solves the linear equations (8) and (9) in spectral space in the horizontal direction and in finite-differences in the vertical direction (Lott, 1998). In time, the evolution equations are solved by one Euler step, followed by successive Leapfrog steps. After each time step, an Asselin filter is applied (Asselin, 1972). The height of the domain is 50 km and its width range between 200 to 1000 km. The horizontal and vertical resolution equals 500 m. At the upper boundary, a damping layer (15 km thick) is used in order to eliminate artificial reflections. The time
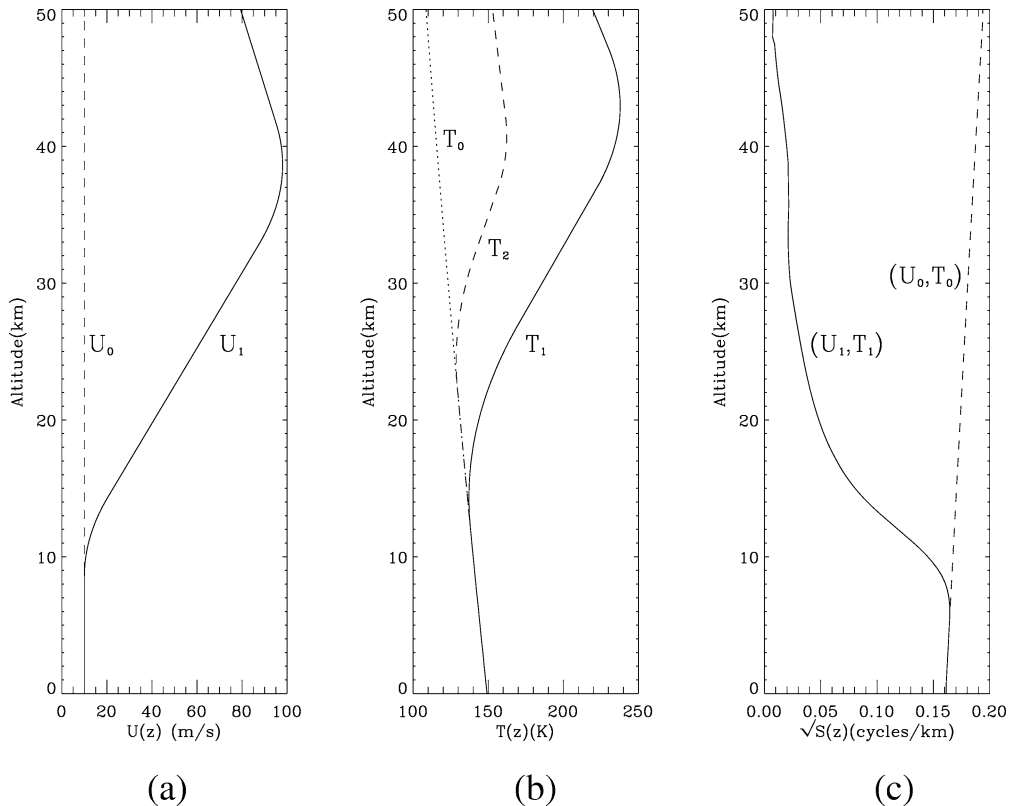

Fig. 1. Background profiles ($U(z)$ and $T(z)$) used for the simulations and the corresponding Scorer parameter profiles ($\sqrt{S(z)}$).

step is equal to 1 s. The background surface pressure is fixed to 7.5 mbar.

2.4. Simulation with an isolated relief

We make here a set of four simulations with an idealized trough, which is characteristic of the north polar cap topography. Its profile is given by:

$$h(x) = -He^{-x^2/L^2}, \tag{14}$$

where H is the depth and L the half width. In all simulations, we take $H = 0.5$ km and $L = 7$ km, values that are characteristic of the troughs in the polar cap according to Ivanov (2000). In the first two simulations, the CO_2 ice condensation is neglected. The background flows are such that in one case, there is no trapped resonant modes (background profile (0)) while in the other case, trapped modes can occur (background profile (1)). The third and fourth simulations repeat the first two, but forbidding the temperature to go below the CO_2 frost point.

2.4.1. Dynamic simulation

Figures 2a and 2b present the velocity and the temperature anomalies field after 4 h of integration and for the background profiles (0) and (1), respectively. On both figures, the wind and temperature fields above the trough present a well defined upward and freely vertically propagating wave, as indicated by the tilt against the background wind of the wave patterns. In these patterns, the positive (negative) temperature anomalies are located above where air descend (ascend), consistent with them being due to adiabatic warming (cooling). Notice that, as altitude increases, the wave amplitude above the trough increases, which is consistent with the fact that the air density decreases with altitude.

The two simulations strongly differ in the lee of the ridge. With constant background wind (profile (0), Fig. 2a), the disturbances downstream are very weak. When the background wind and temperature vary (profile (1), Fig. 2b), the waves extend downstream and the disturbance field in the lee compares in amplitude with its value above the trough. This result comes from the fact that a significant fraction of the harmonics excited at the ground, meets a turning point above $z = 10$ km and can be reflected downstream. In this simulation with profile (1), the wave pattern downstream has a rather well defined horizontal wave length, $\lambda_x \simeq 20$ km. Although the wave pattern downstream is not steady, the dominance of this particular wavelength illustrates the existence of at least one resonance in the background profile (1). However, as the turning level of this mode is quite high ($z \simeq 10$ km), it takes a rather long time to develop and several hours are necessary before it dominates the wave fields downstream.

Since the resonant mode amplitude compares to that of the freely propagating wave, we can assume that the vertical wind amplitude is everywhere given by its value near the ground: $w' \simeq U(0)\partial h(x)/\partial x \simeq U(0)H/L$ (see Eq. (7)). It
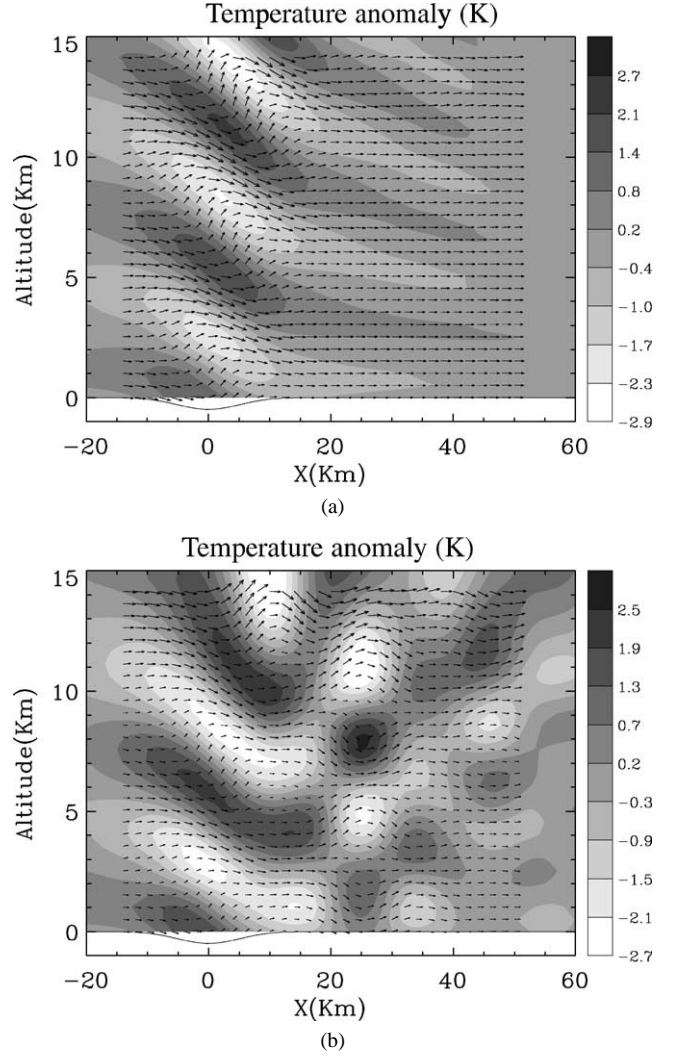

Fig. 2. Wind (arrows) and temperature anomalies (shaded) (K) produced by gravity waves generated by a gaussian trough after $t = 4$ h in a non-condensing atmosphere. The gaussian trough parameters are $H = 0.5$ km and $L = 7$ km. The CO_2 condensation is neglected. (a) Background flow $U(z) = U_0$, $T(z) = T_0$, scale for the wind: $u_{max} = 17$ m s^{-1} (maximum horizontal wind), $w_{max} = 1.7$ m s^{-1} (maximum vertical wind). (b) Background flow $U(z) = U_1$, $T(z) = T_1$, scale for the wind: $u_{max} = 27$ m s^{-1}, $w_{max} = 3.5$ m s^{-1}.

results in temperature variations that are roughly given by $T' \simeq T(0)HN^2/g$ (see Eqs. (5) and (9)), a value consistent with those in Figs. 2a and 2b. If we apply these scalings to the martian north polar cap topography, which is made of successive troughs of characteristic scales, $H = 500$ m and $L = 7$ km (Ivanov, 2000), temperature anomalies of near 2 K can be expected. This value is large enough to force cloud formation.

2.4.2. Impact of the condensation on the wave dynamic

In reality the waves occur in an atmosphere close to the frost point, and the waves are affected by the release of latent heat when CO_2 is condensing. To study this effect, we have reconducted the first two experiments assuming that the
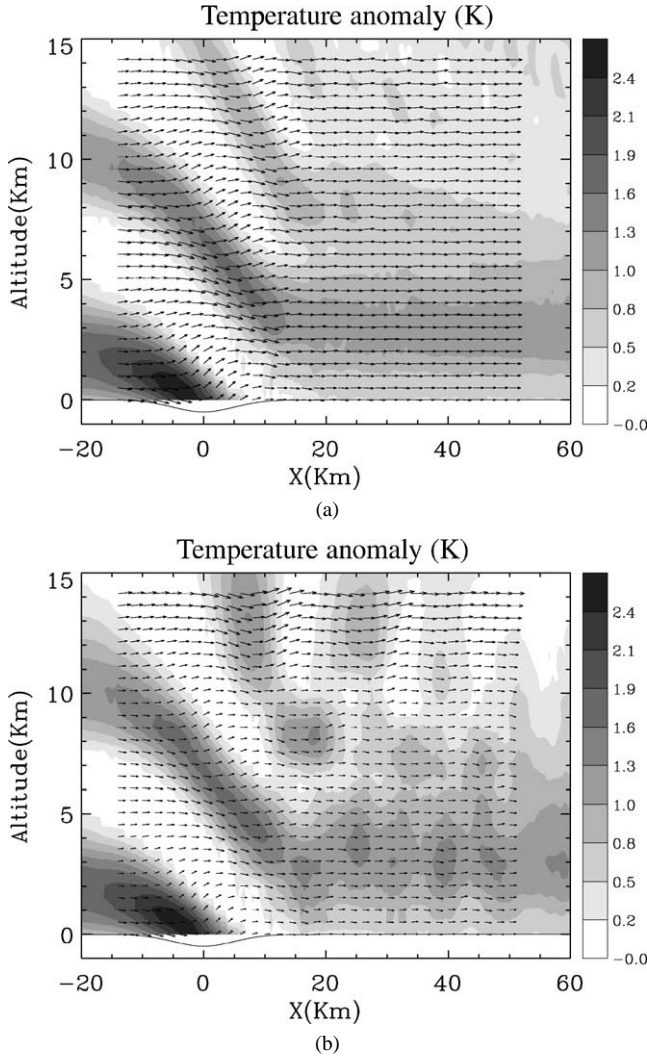
Temperature anomaly (K)

(a)

Temperature anomaly (K)

(b)

Fig. 3. Same as Fig. 2 but with a very simple CO_2 condensation parameterization ($T \geqslant T_{cond}$) (see Section 2.4). (a) Background flow $U(z) = U_0$, $T(z) = T_0$, scale for the wind: $u_{max} = 13$ m s^{-1}, $w_{max} = 1$ m s^{-1}. (b) Background flow $U(z) = U_1$, $T(z) = T_1$, scale for the wind: $u_{max} = 24$ m s^{-1}, $w_{max} = 1.3$ m s^{-1}.

temperature T_{dyn} cannot fall below the condensation temperature T_{cond}. This is an extreme case used to serve as a theoretical basis to understand the impact of CO_2 ice condensation on the dynamics. More realistic cases including simple cloud microphysics are presented in Section 4. Results for the two different background conditions are shown on Figs. 3a and 3b. The impact on the wave field is very strong. Wherever ascent due to wave disturbances tends to produce a cooling below the condensation temperature, CO_2 ice condensation keep the air parcel near T_{cond} which is also the background temperature. The parcel is just as heavy as its environment and no restoring force drives it down.

For this fundamental reason, the disturbance fields in Figs. 3a and 3b only see the ascent and descent near the ground directly forced by the trough. The gravity wave dynamics only act in producing the first descent along the upstream side of the trough (positive temperature anomaly) and

the ascent described before and where the condensation annihilates the wave. Following this picture, it seems natural that the disturbances do not see the background flow variations located above 10 km and the disturbance patterns in Figs. 3a and 3b are near one from the other: the condensation annihilates the resonance.

3. A parameterization of CO_2 ice cloud formation

The above simulations with simplified condensation scheme have proven that the dynamics of mountain waves is strongly affected by the condensation of CO_2, at least within a near saturated atmosphere. Accordingly, a better description of the condensation process including nucleation of the ice particles, growth rate, wind advection and sedimentation, and sublimation, is needed to accurately model the formation of wave clouds as well as the feedback of the condensation–sublimation processes on the wave dynamics. Compared to the results in Section 2, CO_2 ice microphysical processes can indeed delay the onset and the development of CO_2 ice clouds, allowing a more complete development of the gravity waves disturbance.

3.1. Microphysics of CO_2 ice

As for water clouds on Earth, the microphysics of CO_2 ice cloud primarily depend on the supersaturation s ($s > 0$) or subsaturation ($s < 0$) of the atmosphere:

$$s = P_\infty / P_v - 1. \tag{15}$$

In Eq. (15), P_∞ is the ambient partial pressure of CO_2 (on Mars it is near the ambient total pressure), P_v is the equilibrium vapor pressure of CO_2: $P_v = A_{cc} \exp(-B_{cc}/T_\infty)$, with $A_{cc} = 1.382 \times 10^{12}$ Pa and $B_{cc} = 3182.48$ K (James et al., 1992). The formation of ice particles requires some degree of supersaturation. Homogeneous nucleation needs very high supersaturation ($s > 200\%$), while heterogeneous nucleation, which involves a foreign substrate (dust or water ice particle) occurs at relatively low supersaturation. For two reasons, heterogeneous nucleation is likely to occur within the polar night atmosphere. First, the martian northern middle latitudes in fall and winter are often swept by regional dust storms (Cantor et al., 2001), which probably inject a large amount of aerosols into the polar night atmosphere. Second, it is even more likely that water ice coated dust particles (or even almost pure water ice particles) serve as condensation nuclei for the CO_2 ice: the edge of the polar night is known to contain relatively thick water ice clouds (the polar hood) which are probably present in the entire polar night atmosphere see, e.g., Smith et al., 2001b). Thermal infrared observations performed at the limb at 80 °N suggest that water ice particles are present from above 40 km throughout the region where the CO_2 condensation curve is reached, providing a relatively constant source of nuclei for

CO_2 condensation though vertical sedimentation in addition to horizontal transport (Pearl et al., 2001).

On the basis of theoretical consideration based primarily on Gooding (1986) calculations of the crystallographic disregistry between CO_2 and candidate martian dust minerals, Wood (1999) estimates the minimum critical value of nucleation supersaturation s_{nucl}. He showed that, for a typical dust loading of 0.1 µm aerosol particles atmosphere (visible optical depth $\tau_{vis} = 0.1$), heterogeneous nucleation could occur at supersaturation as low as 10%. Experimental studies (Glandorf et al., 2002), in which water ice is used as a nucleator of CO_2 ice, suggest that critical supersaturations of 30–35% are required. In our study, we consider both values (10 and 35%) as possible values for the critical nucleation supersaturation s_{nucl}.

Once nucleation has occurred, the growth of the ice particles is controlled by microphysical processes. In analogy to Ohm's law (MacKenzie and Haynes, 1992), the growth rate of the particle radius r, $\partial r / \partial t$, can be modeled by

$$\frac{\partial r}{\partial t} = \left[s(T, P) - s_{eq}(T, r)\right] / [R_h + R_m + R_k], \qquad (16)$$

where the constants R_h, R_m, and R_k represent the resistances to the growth due to heat transfer, mass transfer and crystal surface kinetic, respectively. In Eq. (16), s_{eq} is the Kelvin correction that accounts for the effect of the particle curvature on the vapor pressure, it is given by

$$s_{eq}(T, r) = \exp(2M\sigma / r\rho_{ice}TR) - 1, \qquad (17)$$

where M is the molecular weight of CO_2, R is the gas constant, ρ_{ice} is the density of the CO_2 ice, and σ is the surface energy of the CO_2 ice crystal. We take $\sigma = \sigma_{111} = 0.080$ J m^{-2}, {111} being the lowest-energy crystallographic face of CO_2 ice (Wood, 1999). Below s_{eq}, the supersaturation s is not large enough for condensation, and sublimation occurs. As CO_2 is the major component of the martian atmosphere, the resistance associated with mass transfer R_m is negligible ($R_m \ll R_h, R_k$). The growth rate depends mainly on the crystal growth mechanism (Wood, 1999). This author has shown that if crystals grow with the Screw Dislocation growth mechanism, the crystal surface kinetic resistance is negligible as well, and the limiting factor is the heat transfer: $R_h \gg R_k$. If they grow with the 2D nucleation growth mechanism, it is the other way round, the surface kinetic is the limiting factor: $R_h \ll R_k$. In fact, this second mechanism requires very high supersaturation, $s \geqslant 200\%$, which is unlikely to be satisfied. Between these two extreme mechanisms, growth mechanism may also be 2D heterogeneous nucleation, stacking fault or other processes. These depend a lot on the crystal structure of both condensation nuclei and CO_2 ice, factors that are not well-documented for the martian atmosphere.

In order to include the effect of CO_2 ice microphysics on the formation of wave clouds, two extreme growth rate scenarios are defined and tested in our 2D model: a fast growth scenario and a slow growth one. These two scenarios give

an assessment of the upper and lower bounds for the growth rate of CO_2 ice particles. In the fast growth scenario, the growth-rate-limiting process is only the heat transfer R_h, and in the slow growth scenario, it is mainly the surface kinetic resistance R_k. In both cases, the heat transfer resistance is estimated with the following formula:

$$R_h = \frac{r\rho_{ice}L}{k_{th}P_v(T)}\left(\frac{\partial P_v}{\partial T}\right), \qquad (18)$$

where k_{th} is the gas thermal conductivity, $k_{th} = \eta C_p / Pr$, where Pr is the Prandtl number, $Pr \simeq 0.8$ (Wood, 1999), η is the dynamic viscosity,

$$\eta = 5/16\sqrt{\pi}\left(\sqrt{m_m kT}/d_{mol}^2\right), \qquad (19)$$

with m_m the CO_2 molecule mass, k the Boltzmann constant, and d_{mol} the CO_2 molecule diameter. The surface kinetic resistance R_k is fixed to zero in the fast growth scenario, and to 10^7 s m^{-1} in the slow growth scenario. Although Eq. (18) is only valid in the continuum regime, i.e., where the diameter of the ice particles is larger than the mean free path of air molecules in the surrounding atmosphere, it is also used in the kinetic regime to give an upper bound for the growth rate of the smallest ice particles.

More quantitatively, the difference between the two scenarios is the growth rate of the ice particles smaller than 20–40 µm. In the slow growth scenario, the growth rate is controlled by the surface kinetic for particles smaller than 20–40 µm, and it is controlled by the heat transfer for larger ice particles. In the fast growth scenario, whatever the size of ice particles is, its growth rate is controlled by heat transfer. As a consequence, the fast growth scenario overestimates the growth rate of ice particles with radius below 10–20 µm, while the slow growth one under-estimates it.

An other process of importance is the coagulation of the CO_2 ice particles as they collide through Brownian motion. At small particle concentrations, coagulation does not have a significant effect on the cloud properties and do not modify the growth of particles. From Rossow (1978), the coagulation time constant for CO_2 ice depends on the concentration of CO_2 ice particles. Assuming that CO_2 ice particles nucleate on airborne (dust and water ice) particles greater than 0.1 µm, the number density of ice particles is directly related to the number density of aerosol particles initially present in the atmosphere.

Table 1 presents the number mixing ratio of the aerosol particles greater than 0.1 µm for different visible optical

Table 1
Number mixing ratio of aerosol particles (per air mass unit) available for nucleation for different visible optical depths

τ, optical depth	N_{aero} (kg^{-1})
0.01 (clear atmosphere)	5×10^7
0.1	5×10^8
1. (dusty atmosphere)	5×10^9

depths assuming an aerosol size distribution as in Ockert-Bell et al. (1997). In this aerosol size distribution, most of the aerosol particles are included below 1 μm. The mean radius of aerosol particles is about 0.5 μm. For a typical dust loading atmosphere ($\tau_{vis} = 0.1$), if all the aerosol particles lead to CO_2 ice particles and grow to 50 μm radius, the coagulation time is around 10^6–10^8 s. As a comparison, the condensation growth time for 50 μm CO_2 ice particles is around 10^2–10^4 s. The coagulation of ice particles is negligible, and the number of ice particles remains constant with time, once they nucleated.

3.2. Basis of wave clouds formation

The fact that the formation of the clouds depends on both wave patterns and CO_2 ice microphysics, is summarized in Fig. 4. Airborne nuclei are advected horizontally by the background flow and cross the orographic waves. When an air parcel loaded with dust or water ice particles passes over a trough, dynamical cooling induced by orographic wave leads to nucleation if the temperature has decayed enough, i.e., if the temperature variation creates supersaturation as high as the critical nucleation supersaturation (s_{nucl}). As here, the background temperature at low altitude follows the CO_2 condensation temperature, the background saturation equals zero and the super(sub)saturation is directly related to the temperature disturbance. For a 2 K temperature perturbation which is a typical temperature disturbance above the north polar cap (Section 2.4), the supersaturation is near 30–35% below 10 km, a value for which nucleation of CO_2 ice particles is possible. The nucleation starts in the windward side of the clouds where condensa-

tion nuclei advected by the mean flow continuously come into.

Once the ice particles have nucleated, they grow more or less quickly depending on the microphysical assumption. The nucleated particles are advected by the wind out of the nucleation front and continue to grow downstream as long as they stay in a region where $s > s_{eq}$. The size of the CO_2 ice particles and consequently their sedimentation velocity depend on the growth rate: for fast growth, large particles are expected, while for slow growth, small ones are expected.

Once outside the condensation area ($s > s_{eq}$), the ice particles start sublimating. On the one hand, if the particles are sufficiently large, they do not entirely sublimate and can fall to the ground. The clouds then look like long "snow" tails (Colaprete et al., 2002). On the other hand, if the particles are small, they weakly precipitate and can totally sublimate downstream of the condensation area, since $s < s_{eq}$ there. The clouds then resemble stationary clouds made of horizontally moving particles. In this circumstance, the shape of the clouds is likely to be imposed by the orographic gravity waves.

3.3. Description of the cloud model

The number mixing ratio of ice particles N_{part} (i.e., particle number per mass unit) remains constant all along the simulation and in the whole domain, it is fixed at the beginning of the simulation. Nevertheless, the amount of CO_2 ice in each elementary square box (500×500 m) varies with time, it depends on the amount of ice advected from or toward the adjacent boxes and on the growth or sublimation rate of the mean ice particle radius, r_{part}, in each box. The initial mean ice particle radius is fixed to 0.5 μm, which is the mean value of the aerosol particle size (Section 3.1). In addition to r_{part}, in each box, CO_2 ice is also described by the mean mixing ratio of CO_2 ice, q, which is the mass ratio between the ice phase and the gaseous phase.

3.3.1. Ice particle transport

The advection of q from a box to the next downstream and below is computed with a Vanleer Scheme (Hourdin and Armengaud, 1999), using the velocity field given by the dynamical part of the model plus a vertical velocity due to the sedimentation of ice particles, V_{sed}. In each box, V_{sed} is derived from the mean ice particle radius r_{part}, by using a Stokes law corrected for low pressure by the Cunningham slip-flow correction (Rossow, 1978). At each time step, the distribution of CO_2 ice mixing ratio q is recalculated with this advection scheme, and a new mean ice particle radius r_{part} is estimated in each box. After that stage, the condensation or sublimation of these ice particles is computed.
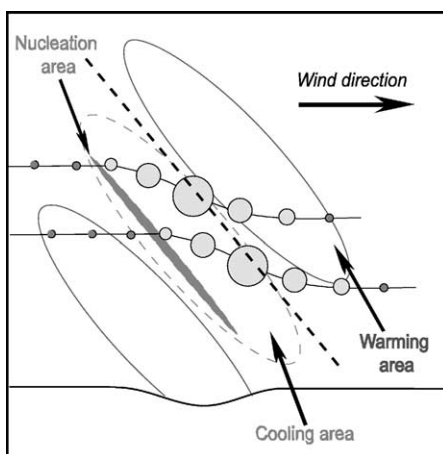

Fig. 4. Schematic drawing describing the wave cloud formation. Dust or water ice particles (dark grey circle) transported by wind cross the stationary gravity wave features. When an aerosol particle comes into the nucleation area ($s > s_{nucl}$), it nucleates and grows as long as it stays in the condensation area ($s > 0$). The more it grows, the more it falls. Once outside the condensation area, the particle starts sublimating. If it sublimates more quickly than it falls, it does not precipitate to the ground and completely sublimates in the atmosphere.

3.3.2. Condensation–sublimation processes

In each box, a value of the supersaturation s_1 is estimated after each dynamical time step, at $t + dt$, using Eq. (15):

$$s_1(t + dt) = P(t + dt)/P_v(t + dt) - 1, \qquad (20)$$

where $P_v(t + dt) = A_{CC}e^{-B_{CC}/(T(t)+(\partial T/\partial t)_{dyn} dt)}$ is the equilibrium vapor pressure (see Section 3.1), P is the ambient pressure, and $(\partial T/\partial t)_{dyn}$ is the dynamical tendency of the temperature deduced from the potential temperature by Eqs. (5) and (9).

On the one hand, if CO_2 ice is advected in the box from its adjacent boxes, the further growth of the mean ice particle radius is allowed, and the growth rate is calculated with Eq. (16). On the other hand, if no CO_2 ice is advected in the box, the condition $s_1 > s_{nucl}$ is required to allow the growth of the mean ice particle radius r_{part}. Indeed, if no CO_2 ice is advected into the box, that means that non-ice particles, which are continuously advected by the mean flow, come into. The growth of these non-ice particles is only possible if the critical nucleation supersaturation s_{nucl} is reached. In fact, $s_1 > s_{nucl}$ should be required only in the windward part of the box, where non-ice particles are concentrated. To accurately describe this phenomenon, a submesh grid would be necessary. But, by simplicity, this requirement is imposed on the whole mesh.

The calculation of the amount of condensed or sublimated CO_2 ice leads to a new value of the super(sub)saturation s_2. If the saturation variation is large, $|s_1 - s_2| > s_1/4$ typically, numerical errors on the condensed or sublimated ice quantity can become significant. To reduce these errors, a physical time substep dt/N is imposed with $N = |s_1 - s_2|/(s_1/4)$. For each time substep, $T(t + dt/N)$ is estimated from the dynamical temperature tendency, constant all along the dynamical time step dt, and from the condensation temperature tendency, which is calculated from the quantity of CO_2 ice condensed (or sublimated) during the previous time substep dt/N:

$$\left(\frac{\partial T}{\partial t}\right)_{cond} = \frac{L}{C_p} \frac{N \, \delta q}{dt}. \qquad (21)$$

In Eq. (21), L is the latent heat of CO_2 ice condensation, C_p is the heat capacity of CO_2 gas, and δq the amount of ice mixing ratio condensed in the previous time substep.

To summarize, the input data of the cloud model are:

1. The critical nucleation supersaturation s_{nucl} and the number mixing ratio N_{part} of ice particles that are allowed to grow.
2. The dynamical temperature tendency $(\partial T/\partial t)_{dyn}$, the pressure P, the temperature T, the vertical and horizontal wind velocities at each time step dt.

The output data is the temperature after condensation T^*, the ice particle radius r_{part}, and the ice mixing ratio q.

4. Results

4.1. Simulations with a 2D-isolated trough

In a first set of experiments, we study the formation of wave clouds over the 2D-isolated gaussian trough used in Section 2 and investigate the sensitivity of the results to (i) the different microphysical assumptions (see Section 3.1) and (ii) the assumed background flows (see Section 2.2.2). To establish if the clouds are optically dense enough to reflect the MOLA laser beam, we follow Pettengill and Ford (2000) and compare the model particle number density to the value,

$$N_{refl} = 2.10^{-8} r^{-2} (m^{-3}), \qquad (22)$$

where r is the particle radius in μm. The first level, starting from the top, where the ice particle number density $N^*_{part} = \rho N_{part}$ (ρ is the air density) is above that threshold, is considered as the Laser reflecting level.

4.1.1. Baseline case

Figure 5a shows the temperature and velocity anomalies field for the background flow profiles (0) ($U = U_0$ and $T = T_{cond}$), in the case of the fast growth scenario with $s_{nucl} = 10\%$ and $N_{part} = 10^7$ kg^{-1}. Like in the simulations with a simple condensation parameterization (Fig. 3), the cloud formation has a strong impact on the wave field. Nevertheless, the inclusion of the realistic microphysics make the resulting wave and cloud fields quite different from those presented in Section 2. The successive condensation and sublimation of the ice particles blown by the wind create a large area where the temperature disturbance is near zero because $T = T_{cond}$. Both condensation and sublimation annihilate the gravity waves far above and downstream the trough.

The four pictures on Fig. 6 present successive phases ($t = 50, 100, 150$ and 200 min) of the development of the cloud features corresponding to Fig. 5a. In all the figures, the black crosses represent the altitude of the expected MOLA echoes, according to Eq. (22). These four successive snapshots show that the wave perturbations increase in amplitude above the trough in function of time. Nevertheless, this growth is rapidly limited by the development of the clouds.

After $t = 50$ mn (Fig. 6a), the wave perturbations have propagated upward and the supersaturation has reached the critical nucleation supersaturation s_{nucl} between 1 and 3 km above the trough. At that time (Fig. 6a), a small cloud has already formed. Where the ice particles start growing, supersaturation decreases, except in a narrow band on the windward side of the cloud. In this band, supersaturation remains quite high and allows the non-ice particles to start growing. The supersaturation in the cloud rapidly falls to $\simeq 0\%$. The ice particles stop to grow, and they are just advected by the wind and fall down. The ice particles sublimate downstream where $s < s_{eq}$, which limits the horizontal extension of the
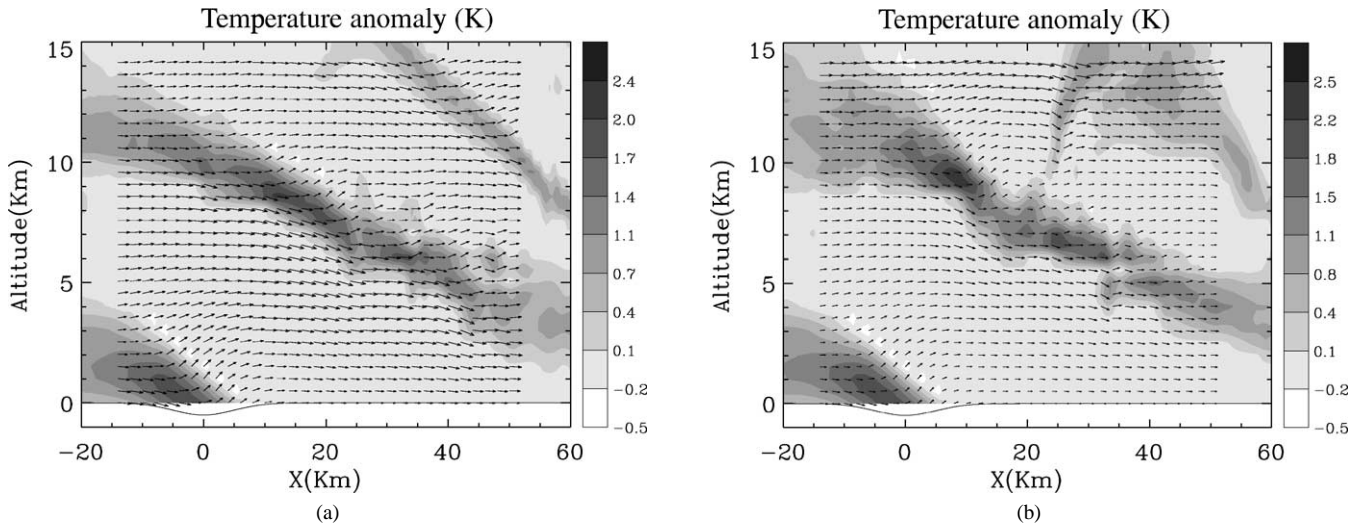
Fig. 5. Same as Figs. 2 and 3 but with a more realistic microphysical parameterization: fast growth scenario, $N_{part} = 10^7$ kg^{-1}, $s_{nucl} = 10\%$. The gaussian trough parameters are $H = 0.5$ km and $L = 7$ km. Left panel (a): background flow $U(z) = U_0$, $T(z) = T_0$, scale for the wind: $u_{max} = 14$ m s^{-1}, $w_{max} = 1$ m s^{-1}. Right panel (b): background flow $U(z) = U_1$, $T(z) = T_1$, scale for the wind: $u_{max} = 24.5$ m s^{-1}, $w_{max} = 1.4$ m s^{-1}.
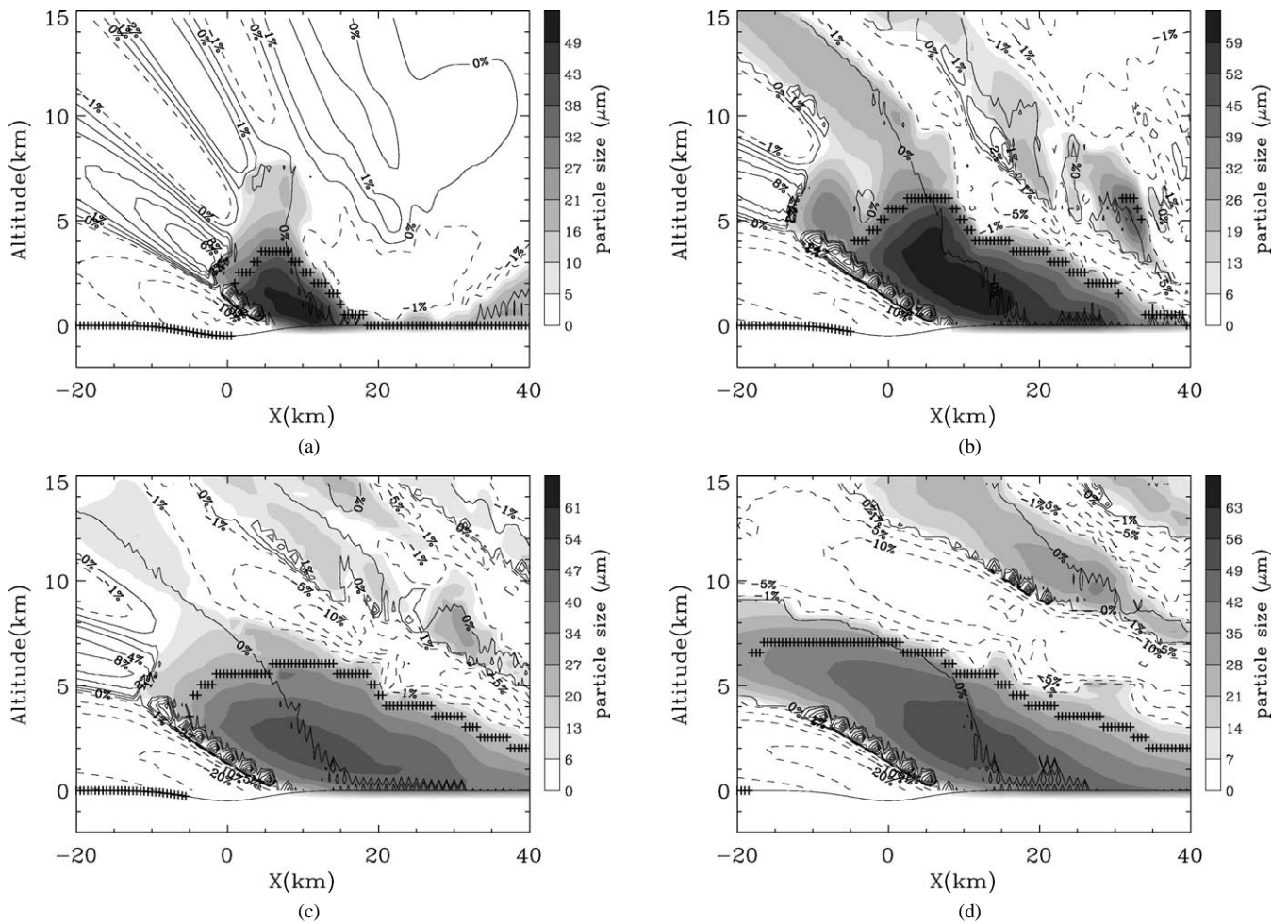

Fig. 6. Different stages of the wave cloud formation. This simulation was performed with a constant wind profile $U_0 = 10$ m s^{-1} and the T_0 temperature profile, for $N_{part} = 10^7$ kg^{-1}, $s_{nucl} = 10\%$, and for the fast growth scenario. Shaded contours represent CO_2 ice particle radius (μm). Contour plots represent supersaturation and subsaturation (plane and dashed line). Black crosses are the simulated cloud MOLA echoes. The wind blows from the left to the right.

Table 2
Characteristics of the cloud obtained above a 2D-isolated trough ($H = 0.5$ km, $L = 7$ km) after 4 h of integration, assuming the fast growth scenario (see Section 3.1), with a constant wind U_0 (5 or 10 m s^{-1}) profile and CO_2 condensation temperature profile (T_0)

N_{part} (kg^{-1})	1e5	1e5	1e6	1e6	1e7	1e7	1e8
s_{nucl}	10%	35%	10%	35%	10%	35%	10%
MOLA detectability ($U_0 = 5$ m s^{-1})	–	–	✓	–	✓	–	✓
MOLA detectability ($U_0 = 10$ m s^{-1})	–	–	✓	✓	✓	✓	✓
R_{max} (µm) ($U_0 = 5$ m s^{-1})	130	–	90	–	62	–	29
R_{max} (µm) ($U_0 = 10$ m s^{-1})	185	180	112	115	64	62	30
δ_{cloud} ($U_0 = 5$ m s^{-1})	–	–	4°	–	6°	–	$\simeq 0°$
δ_{cloud} ($U_0 = 10$ m s^{-1})	–	–	7°	8.5°	12°	9.5°	$\simeq 0°$
ve_{cloud} (km) ($U_0 = 5$ m s^{-1})	–	–	1	–	4	–	7
ve_{cloud} (km) ($U_0 = 10$ m s^{-1})	–	–	4.5	4.5	9	10	11

The ice particle number mixing ratio N_{part} (kg^{-1}) and the critical nucleation supersaturation s_{nucl} are fixed at the beginning of the simulation. The MOLA detectability of the simulated cloud is indicated by a tick. R_{max} is the maximal value of the mean ice particle radius, δ_{cloud} is the slope of the cloud echoes, and ve_{cloud} is their vertical extension, i.e., the distance between their base and their top. The clouds are detectable only for $N_{part} \geqslant 10^6$ kg^{-1}. For $s_{nucl} = 35\%$ and $U_0 = 5$ m s^{-1}, the supersaturation is not high enough for nucleation to occur.

cloud. Before starting to sublimate, the mean ice particle radius within the cloud reaches about 60 µm.

After 100 min (Fig. 6b), a large cloud is formed. Above this primary cloud, other clouds develop as well. As they are made of smaller particles than the primary low level cloud and as the number density N^*_{part} of particles decreases with altitude, they remain undetectable. Only the main extended cloud near aloft the trough is detectable by MOLA.

Thereafter, this primary cloud keeps growing (Fig. 6c) and, at $t = 200$ mn (Fig. 6d), a sloping cloud extended from the surface to near 7 km above it, is obtained. The slope of its echoes δ_{cloud} is near 8°, a value close to the echoes of isolated clouds observed by the MOLA experiment (see Table 3 in Pettengill and Ford (2000) for a comparison). It is noteworthy that the model cloud echoes do not necessarily correspond to the top of the cloud but to a region within the cloud where the ice particles are large and dense enough to backscatter the Laser pulse at a level detectable by MOLA. Nevertheless, the shape of the echo backscatters is directly related to the cloud shape. Note as well that the cloud and the echoes are tilted against the wind direction, following the vertically propagating gravity wave.

4.1.2. Sensitivity to background conditions

Figures 5a and 5b show model results for the background flow profiles (0) and (1), respectively, with $U_0 = 10$ m s^{-1}, after 4 h of integration. The comparison between these two figures shows that the presence of a wind shear at middle altitude (wind profile (1)) has no influence on the wave field pattern. This follows that the waves are strongly damped at low altitude, so they mainly produce an extended detectable cloud above the trough. At altitudes higher than 10 km above the surface, the wave pattern and the cloud shape are near indistinguishable, only the main cloud at low altitude is detectable, and the echoes are almost the same for the two background conditions (not shown in Fig. 5 but they are those presented in Figs. 6d and 7d).

Table 2 presents the general characteristics of the extended cloud (its MOLA detectability, its maximum value of the mean ice particle radius, R_{max}, the slope of its echoes, δ_{cloud}, and the vertical extension of the echoes, ve_{cloud}, i.e., the vertical distance between the base and the top of its echoes) obtained for different input parameters. The results corresponding to Fig. 6 are presented in column 5. These show that simulations performed with two different values for the low altitude wind amplitude ($U_0 = 5$ m s^{-1} or $U_0 = 10$ m s^{-1}) lead to different echo features. For $U_0 = 10$ m s^{-1}, the cloud echoes are more extended and more sloping than for $U_0 = 5$ m s^{-1}.

We then made sensitivity tests to different altitudes of the polar thermal inversion: 12.5, 25 and 50 km, corresponding to the temperature profiles T_1, T_2 and T_0, respectively. The maximum altitude of cloud formation is sensitive to the inversion altitude, but the maximum altitude of cloud echoes does not depend on it: all cloud echoes are obtained below altitudes of 15–20 km above the surface.

4.1.3. Sensitivity to microphysical parameters

To examine the robustness of our results, sensitivity tests to values of the critical nucleation supersaturation s_{nucl} and of the number mixing ratio N_{part} of ice particles, and to the growth scenario (slow or fast) have been made. In all the cases presented in this section, those tests are limited to the uniform background profiles (0).

Critical nucleation supersaturation s_{nucl}. Figure 7 presents the time evolution of cloud formation corresponding to Fig. 6, i.e., with $N_{part} = 10^7$ kg^{-1}, for the fast grow scenario, but with $s_{nucl} = 35\%$. Comparison with Fig. 6 shows that a higher critical nucleation supersaturation delays the onset of cloud formation by about 100 min. This delay permits a larger development of the wave fields (Fig. 7a) and consequently modifies slightly the resulting cloud pattern. Figure 7b show that nucleation starts after about
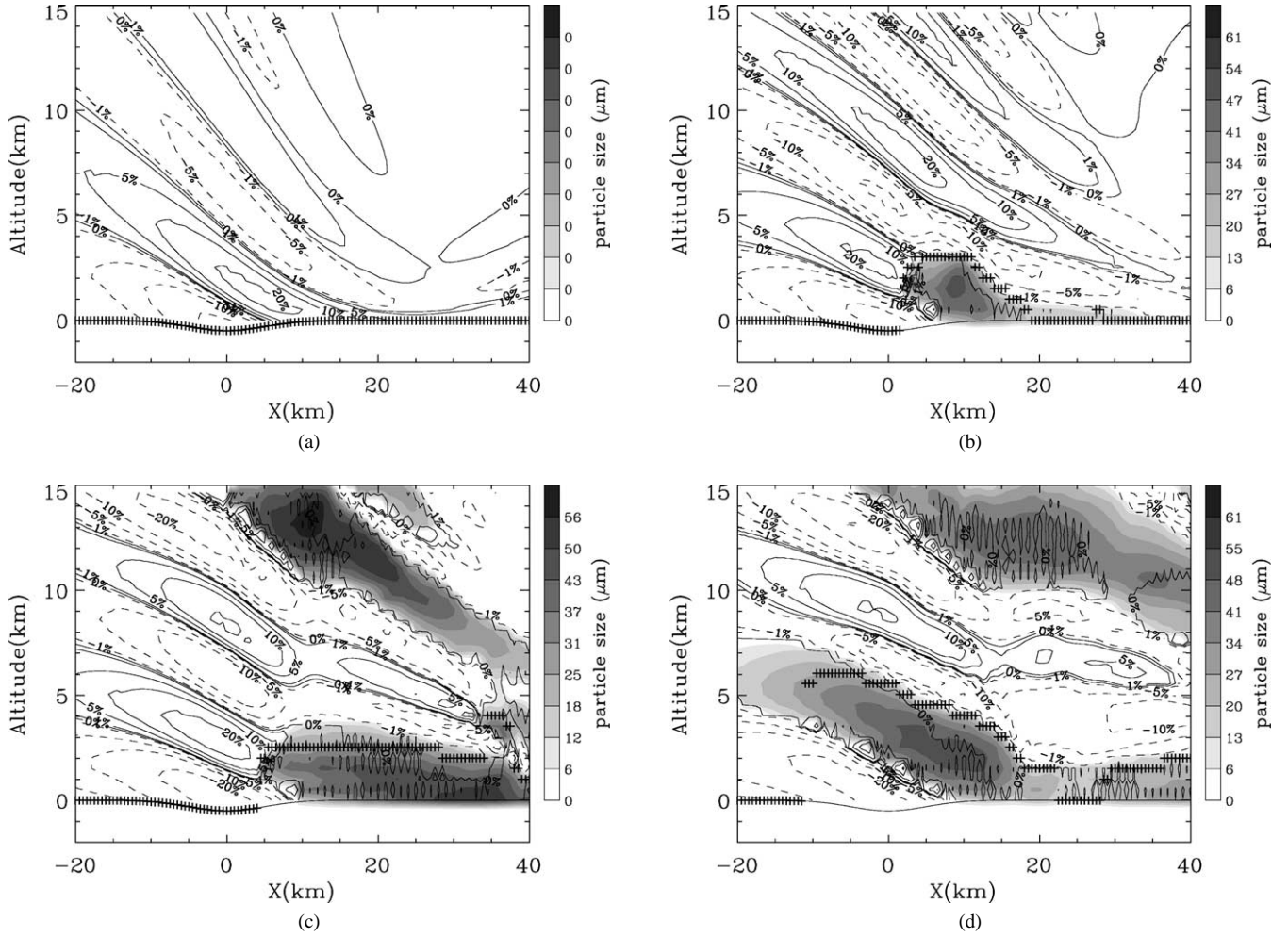
Fig. 7. Same as Fig. 6 with $s_{nucl} = 35\%$.

100 min only, between 1 and 3 km above the trough, like in Fig. 6a. After 150 min (Fig. 7c), a second cloud appears between 10 and 15 km above the surface. After 200 min (Fig. 7d), an extended cloud is formed above the trough. It produces echoes from the ground up to a altitude of 6 km. The slope of the echo feature is around 9–10°. Like in the simulation with $s_{nucl} = 10\%$ (Fig. 6), the higher altitude clouds are not detectable by the MOLA instrument.

The general characteristics of the resulting cloud are summarized in column 5 and 6 of Table 2, for the runs in Figs. 6 and 7, respectively. For these two cases, the maximal value of the mean ice particle radius R_{max}, the vertical extension ve_{cloud} of the echoes and their slope δ_{cloud} do not significantly depend on s_{nucl}. This result is quite systematic (see the other columns in Tables 2 and 3), note nevertheless that when $s_{nucl} = 35\%$ and for $U_0 = 5 \, \text{m s}^{-1}$, no clouds are formed (i.e., there are no assigned values to R_{max}, δ_{cloud} and ve_{cloud} for these input values). This comes from the fact that supersaturation never exceeds the threshold for particles to start growing, at least after 4 h of integration.

Ice particle number mixing ratio N_{part}. It is clear from the first two columns in Table 2 that one needs $N_{part} > 10^5 \, \text{kg}^{-1}$ to obtain detectable clouds. For the slow growth scenario (Table 3), one needs $N_{part} > 5 \times 10^6 \, \text{kg}^{-1}$. Note as well that for increasing ice particle number mixing ratio N_{part}, the maximum ice particle radius, R_{max}, and the cloud slope, δ_{cloud}, decrease (see the raws 3, 4, 5 and 6 in Tables 2 and 3). In the fast growth case, for $N_{part} \geqslant 10^8 \, \text{kg}^{-1}$, the cloud feature corresponds to a haze transported by the wind ($\delta_{cloud} \simeq 0°$). In this case, no clouds with sloping top form, the nucleated ice particle number mixing ratio is too large, so the release of latent heat when they nucleate and start growing is very strong and the wave perturbation is completely attenuated downstream . In the slow growth scenario (Table 3), the same kind of results is obtained for $N_{part} \geqslant 5 \times 10^9 \, \text{kg}^{-1}$. It is one of the few circumstances where the modeled clouds do not have the characteristics of the observed isolated clouds (Pettengill and Ford, 2000; Ivanov and Muhleman, 2001), while for $10^6 < N_{part} < 5 \times 10^7 \, \text{kg}^{-1}$ with the fast growth scenario, the model cloud echoes are similar to the observed ones.

Table 3
Same as Table 2 but assuming the slow growth scenario (see Section 3.1)

N_{part} (kg^{-1})	5e6	5e6	5e7	5e7	5e8	5e8	5e9
s_{nucl}	10%	35%	10%	35%	10%	35%	10%
MOLA detectability ($U_0 = 5$ m s^{-1})	–	–	√	–	√	–	√
MOLA detectability ($U_0 = 10$ m s^{-1})	–	–	√	√	√	√	√
R_{max} (µm) ($U_0 = 5$ m s^{-1})	28	–	23	–	11	–	6.5
R_{max} (µm) ($U_0 = 10$ m s^{-1})	29	–	22	21	12	11	6
δ_{cloud} ($U_0 = 5$ m s^{-1})	–	–	5°	–	2°	–	≃ 0°
δ_{cloud} ($U_0 = 10$ m s^{-1})	–	–	5°	5°	≃ 0°	4°	≃ 0°
ve_{cloud} (km) ($U_0 = 5$ m s^{-1})	–	–	2.5	–	4	–	6.5
ve_{cloud} (km) ($U_0 = 10$ m s^{-1})	–	–	5	6	6	15	20

Growth rate: fast or slow. The comparison between Table 2 (fast) and Table 3 (slow) shows that the maximal value of the mean ice particle radius, R_{max}, depends strongly on the growth limiting factor. R_{max} is quite systematically larger, for the fast growth scenario (Table 2) than for the slow growth scenario (Table 3). Accordingly, in the fast growth case (Table 2), less ice particles ($N_{part} \geqslant 10^6$ kg^{-1}) are needed for the detection by MOLA than in the slow growth case ($N_{part} \geqslant 5 \times 10^7$ kg^{-1}). Note as well that the slope of the cloud echoes is higher for the fast growth scenario because the ice particles are larger and consequently sedimentate more. Nevertheless, even in this case, there is only a small amount of ice that falls down to the ground. In the slow growth scenario, the ice particle transport is mainly controlled by horizontal advection, making the slopes rather small. In this scenario, it is difficult to obtain slopes near the 15°–20° observed by MOLA (Ivanov and Muhleman, 2001).

4.1.4. Summary of the isolated trough simulations

The above simulations have shown that the clouds triggered by a single trough are near always tilted against the wind, at least the primary cloud below $z = 10$ km, i.e., within the layer where the wind is constant. This primary cloud is related to vertically propagating gravity waves forced by the trough and extents from the surface up to $z = 3–7$ km. Above this primary cloud near the surface, other clouds at higher altitudes are generally found, but they cannot be detected by MOLA, at least for realistic number mixing ratio of ice particles ($N_{part} < 10^9$ kg^{-1}). There is also a lower limit, around 10^6 kg^{-1}, for the ice particle number mixing ratio for the detectability of the primary cloud by MOLA. The slope of the primary cloud echoes corresponds to the slope of the cloud but does not necessarily correspond to the top of the cloud. These last results are not much sensitive to the background flow profiles above 10 km and to the critical value of the nucleation supersaturation, s_{nucl}: whatever this value is, the temperature anomalies induced by a 10 m s^{-1} wind over a 0.5 km depth trough in an atmosphere with $T \sim T_{cond}$ are large enough to create CO_2 ice clouds below 20 km. The vertical extension and the slope of the echoes mainly depend on both the growth rate assumption and on the wind amplitude at low level. In the fast growth scenario, the cloud echoes are more inclined than in the slow growth scenario. The wind amplitude at low altitude also increases the slope and the vertical extension of the clouds. The simulated cloud echoes formed above a idealized single trough successfully reproduce the echoes of the isolated clouds observed by the MOLA experiment (Pettengill and Ford, 2000). Finally, these simulations have also allowed us to constrain the values of the model parameters, before proceeding to simulations with realistic north polar cap topographies.

4.2. Simulation with realistic topographies

In this section, the wave cloud model is used in the presence of realistic topographies, and even more quantitative comparisons with the MOLA observations are made. As the simulation in Section 4.1 only reveal a weak sensitivity of the model response to the background flow structure above 12.5 km, simulations with profiles (0) only are presented in the next three subsections. Three topography profiles that correspond roughly to the three MOLA observations: Passes 207, 260 (Pettengill and Ford, 2000), and 222 (Ivanov, 2000) are considered. Note however that the exact topography that triggered the clouds cannot be used since the exact direction of the wind is not known. Nevertheless, the global direction of the wind which corresponds to the three MOLA observations can be estimated from the shape of the cloud echoes (if we assumed that they are tilted against the wind, see Section 4.1.4). On this basis, the wind direction will lead to a large-scale upslope air ascent for Pass 222 (Fig. 9) and to a large-scale downslope air descent for Pass 207 (Fig. 10). Large scale cooling and warming will be induced by these large-scale upslope and downslope air motion, respectively (Forget et al., 1998).

4.2.1. Large-scale flat topography

Figure 8 compares the MOLA observations (upper panel) for Pass 260, with the simulated clouds and echoes after 2 h of integration (lower panel). On this figure and for com-
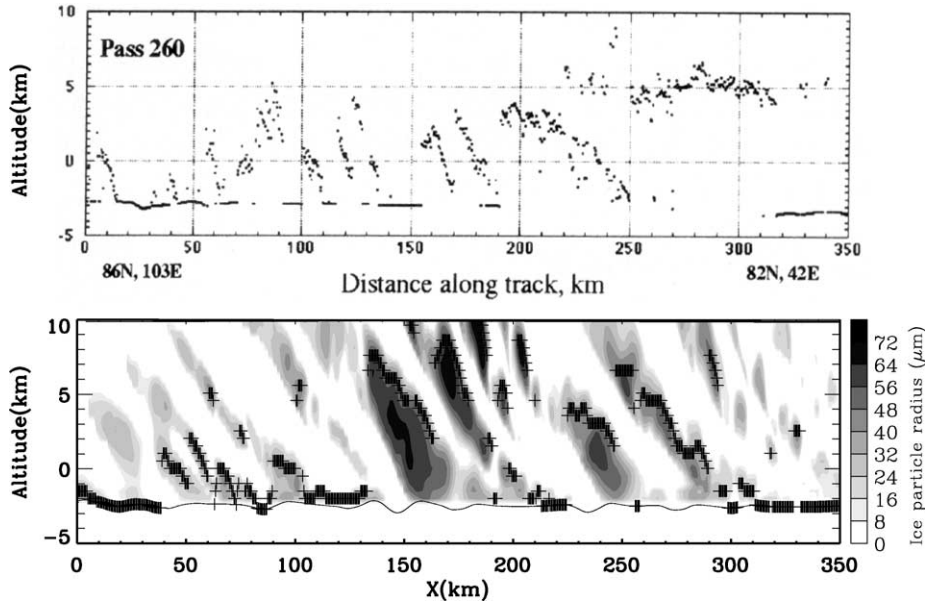
Fig. 8. Comparison between MOLA observations (Pass 260, Pettengill and Ford, 2000) (top) and wave cloud simulation (bottom) performed with a large scale flat topography for the following background conditions: $U_0 = 10 \ \mathrm{m \ s}^{-1}$, $T = T_{\mathrm{cond}}$ (T_0), and microphysical parameters: $N_{\mathrm{part}} = 10^7 \ \mathrm{kg}^{-1}$, $s_{\mathrm{nucl}} = 10\%$, fast growth, after 2 h of integration. Shaded contours represent CO_2 ice particle radius (μm). The black crosses are the simulated cloud echoes. The wind blows from the left to the right.

parison with the MOLA data, the altitude is defined as the altitude above the 6 mbar reference level, contrary to the results presented in the previous section, where the altitude was the distance from the surface. Above each trough or ridge, at low altitude, extended sloping clouds are formed, they resemble to the clouds in the single trough simulation (compare for instance the thick clouds near $x = 150$ km and $x = 250$ km in Fig. 8 to that in Fig. 6d). Nevertheless, as they are induced by higher topography, they are a little bit more extended and made of larger particles than in Section 4.1 ($R_{\mathrm{max}} = 72$ μm instead of 61 μm in Fig. 6d). Above these low-level clouds, secondary clouds are also formed, and contrary to the simulation with a single trough, some of them are now detectable by MOLA. Their detectability once again comes from the fact that they are made of larger particles than in the single trough simulations. These clouds also seem to be directly related to the underlying relief, not to trapped resonant waves.

The horizontal extension of the wave induced clouds and the radius of the ice particles depend on the topography amplitude variation. For instance, the cloud above the trough at $x = 150$ km is more extended and made of larger particles than the one above $x = 250$ km, because the trough at $x = 150$ km is larger and deeper than at $x = 250$ km. Furthermore, no large low level clouds are formed between these two points, because the topography variation are not very pronounced. This result plus the fact that there is no preferential horizontal wavelength in Fig. 8, witness again that the succession of the clouds results from the succession of troughs and ridges rather than from the presence of trapped lee waves.

4.2.2. Large-scale upslope air motion

Figure 9 compares the MOLA observations (upper panels) for Pass 222, with the simulated clouds and echoes after 4 h of integration (lower panels). The large-scale upslope air motion induces a large-scale adiabatic cooling and creates a large amount of CO_2 ice. Nevertheless, this large-scale CO_2 cloud is modulated by small-scale cooling and warming areas due to the smaller scale topographic variations. After 4 h of integration, a good agreement between the simulated echoes and the observed one is obtained. Like in the flat case, the most extended clouds, which are composed of the largest ice particles, are located immediately above and downstream the deepest troughs (see for instance at latitude $= 83°$ on the lower right hand picture on Fig. 9).

Large-scale downslope air motion. Figure 10 compares the MOLA observations (upper panel) for Pass 207, with the simulated clouds and echoes after 5 h of integration (lower panel). The large-scale adiabatic warming induced by the downslope air motion prevents the formation of ice particles at low altitude. In this case, and for $x \geqslant 100$ km, the ice particles which are formed more than 3 km above the surface sublimate before they reach the ground. Simulated cloud echoes also compare very well with the observed ones: no cloud echoes (or just a few echoes) are found between the surface and 3–4 km above; the vertical extension and the slope (between $10°$ and $20°$) of the cloud echoes are relatively similar to the observed ones. Note as well that the simulated cloud echoes are generally tilted against the wind direction, as in the single trough simulations. Nevertheless, in some places, like for instance at $x = 400$ km, one cloud looks tilted in the other direction.
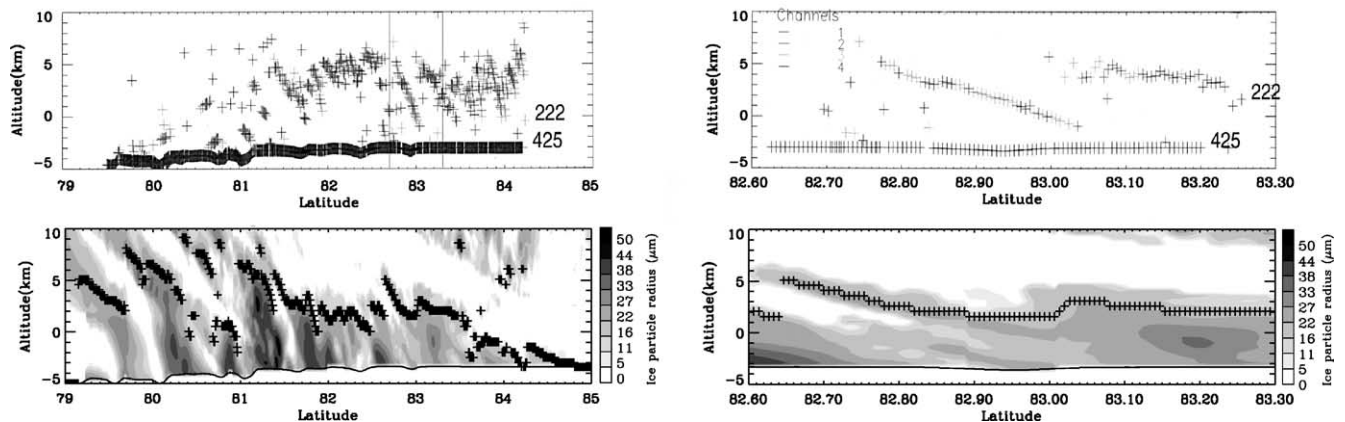
Fig. 9. Comparison between MOLA observation (Pass 222, Ivanov, 2000) (top) and wave cloud simulation (bottom) performed with a large scale upslope topography for the following background conditions: $U_0 = 10 \text{ m s}^{-1}$, $T = T_{cond}$, and microphysical parameters: $N_{part} = 5 \times 10^7 \text{ kg}^{-1}$, $s_{nucl} = 35\%$, fast growth, after 4 h of integration. The topography profile is taken from Pass 425, which was not obscured by clouds and lies adjacent to the track 222. Shaded contours represent CO_2 ice particle radius r_{part} (µm). The black crosses are the simulated cloud echoes. The right panels show a fine detail of the left panels. The wind blows from the left to the right.
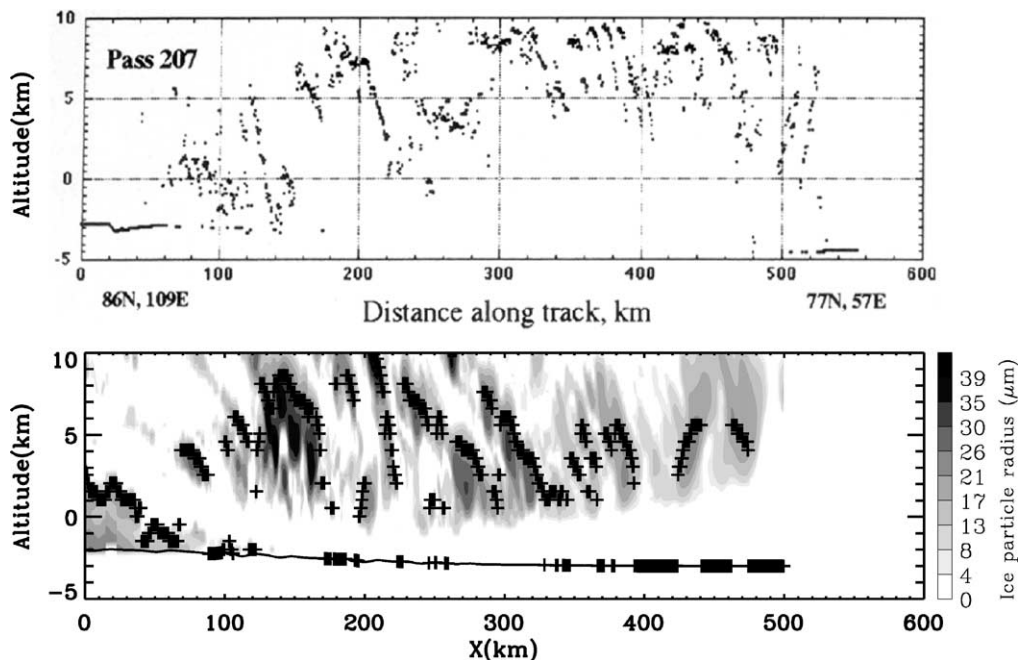

Fig. 10. Comparison between MOLA observations (Pass 207, Pettengill and Ford, 2000) (top) and wave cloud simulation (bottom) performed with a large scale downslope topography for the following background conditions: $U_0 = 10 \text{ m s}^{-1}$, $T = T_{cond}$, and microphysical parameters: $N_{part} = 5 \times 10^7 \text{ kg}^{-1}$, $s_{nucl} = 10\%$, fast growth, after 5 h of integration. Shaded contours represent CO_2 ice particle radius (µm). The black crosses are the simulated cloud echoes. The wind blows from the left to the right.

Sensitivity to model parameters. The influence of the different background and microphysical parameters on our findings have been systematically tested. In near all the cases, the model predicts cloud echoes relatively similar to the observed ones. Nevertheless, for $N_{part} < 10^6 \text{ kg}^{-1}$, clouds are not detectable, like in the isolated trough case in Section 4.1. Furthermore, we confirm that the occurrence of a wind gradient above 10 km and the altitude of the thermal inversion have no significant influence on the obtained cloud echo features, again like in the single

trough simulations of Section 4.1. The maximum altitude of cloud formation depends on the altitude of thermal inversion, but for a realistic ice particle number mixing ratio ($N_{part} < 10^8 \text{ kg}^{-1}$), the maximum altitude of the cloud echoes does not depend on it: it is always near 15 km above the surface. For completeness, note as well that for the three passes considered, the best agreement between the simulated cloud echoes and the observed ones is obtained for the fast growth scenario, $N_{part} \simeq 1–5 \times 10^7 \text{ kg}^{-1}$, and with $U_0 = 10 \text{ m s}^{-1}$.

5. Discussion and conclusion

Observations with the Mars Orbiter Laser Altimeter experiment have revealed the presence of CO_2 ice clouds in the polar night. Most of the observed clouds show characteristics suggesting that they are triggered by vertically propagating gravity waves. The apparent horizontal periodicity of the cloud echoes even suggests that trapped lee waves structure them. To address these issues, we have developed a mountain wave CO_2-ice cloud coupled model in order to simulate wave cloud formation in the martian polar night.

The simulations show that CO_2 ice particles can nucleate at any altitudes, from the surface up to the altitude of the polar night thermal inversion, when the atmosphere is close to the frost point. Nucleation indeed requires negative temperature perturbations, that are always induced by the topographic troughs and winds at the ground, characteristics of the martian northern polar cap. For a 10 m s^{-1} surface wind (which is a typical value according to the LMD GCM data), ice particles can nucleate below 10 km for critical nucleation supersaturation $s_{\text{nucl}} = 10\%$ or 35%, and for any characteristic polar cap topographic profile. In this condition, a main extended cloud is formed between the surface up to altitudes as high as 8–10 km above any trough, characteristic of the polar cap orography.

In our model, the apparently periodic cloud features are not the consequence of an unique atmospheric resonant gravity wave, but of successive gravity waves, each generated by successive individual troughs. First, and although resonance can take place in the absence of CO_2 condensation in the case of a wind profile with high altitude gradient (U_1), the resonance that can occur in that case takes a long time to take place and is not really efficient. Second, the supersaturation reaches the critical value for the nucleation quite rapidly above the first trough. Once nucleation occurs, the release of CO_2 condensation latent heat attenuates the buoyancy force and damps the wave perturbations. This second effect strongly inhibits the emergence of resonant trapped modes.

The choice of the temperature profile (T_0, T_1 or T_2) has no consequence on the wave dynamics at low altitude (below 15 km). However, it is essential for cloud formation at higher altitudes. The maximum cloud formation altitude indeed corresponds to the thermal inversion altitude, but above 15 km, the clouds remain undetectable by the MOLA experiment. This follows the assumption that the ice particle number density decreases with altitude, as the air density decreases. Depending on the assumed particle growth rate (fast or growth), it also exists a lower limit for the detection of low level clouds. For $N_{\text{part}} \leqslant 10^6$–$10^7 \text{ kg}^{-1}$, which correspond to number densities $N_{\text{part}}^* = 2.5 \times 10^4$–$2.5 \times 10^5 \text{ m}^{-3}$ near the surface, even low level extended clouds cannot be detected by MOLA.

Simulations with realistic topography profiles show that the polar cap orography induces both small-scale and large-scale dynamical cooling and warming. On the one hand, when the wind is directed upslope of the polar cap (Pass 222, Fig. 9), air condenses globally. A large-scale cloud is then created, but it is modulated by smaller-scale wave motions. In this case, nevertheless, the large scale cloud makes that a large amount of ice particles precipitates to the ground. On the other hand, when the wind blows downslope, air is globally warmed. Small-scale topography variations generate small cooling areas, and the nucleation of CO_2 ice particles occurs at altitudes higher than 3–5 km above the surface. In this case, the large-scale downslope warming sublimate most of the ice particles before they reach the ground, and the sloping clouds are found between 5 and 10 km above the surface.

Whatever topography profiles and passes are considered, optically thick CO_2 ice clouds with large vertical extension are obtained in our model. They are generally tilted against the background wind direction. Their slope corresponds almost to that induced by upward freely propagating gravity waves. Gravity waves induced by a topography variation (trough or ridge) firstly propagate upward and make cooling and warming areas tilted against the wind direction. As the CO_2 condensation and sublimation strongly damp the wave disturbance, a single topography variation mainly acts in producing few condensation areas between the surface and the altitude of the polar thermal inversion. As in the case with a single trough, resonant trapped lee waves do not seem to play an important role. The location and the size of the clouds are mainly dependent on topography profiles. On the other hand, the slope of cloud echoes mainly depends on the microphysical parameters and the low altitude wind amplitude. The comparison between the simulated cloud echo features and the MOLA echo features (Passes 207, 260 and 222) gives best agreements for the fast growth scenario, $N_{\text{part}} \simeq 1$–$5 \times 10^7 \text{ kg}^{-1}$, and $U(0) = 10 \text{ m s}^{-1}$.

According to our model, we conclude that the observed clouds are quasi-stationary clouds made of moving ice particles ($R_{\text{max}} = 50$–100 μm) that grow and sublimate successively by crossing cooling and warming area induced by the succession of polar cap troughs. The nucleation of ice particles occurs in the upstream side of the clouds, and only a portion of the ice particles precipitates to the ground. The release and absorption of latent heat damp the waves perturbation and prevent resonant trapped wave mode to take place. The apparent periodicity of the observed clouds is linked to the periodicity of the north polar cap troughs. The particular structure of polar night atmosphere is responsible of the cloud slope and their high vertical extension. The slope of the cloud echoes is largely independent of the topography but does depend significantly on the microphysical processes and parameters. The slope of echoes is related to the slope of the clouds, but does not correspond necessarily with the top of the clouds. The cloud shape is linked to the wave pattern, so that the clouds are generally tilted against the background wind direction.

Acknowledgments

References

Asselin, J.M., 1972. Frequency filter for time integrations. Mon. Weather Rev. 100, 487–490.

Cantor, B.A., James, P.B., Caplinger, M., Wolff, M.J., 2001. Martian dust storms: 1999 Mars Orbiter Camera observations. J. Geophys. Res. 106, 23653–23688.

Colaprete, A.T., Owen, B., 2002. Carbon dioxide snow storms during the polar night on Mars. J. Geophys. Res., doi:10.1029/2001JE001758.

Forget, F., Pollack, J.B., Hansen, G.B., 1995. Low brightness temperatures of martian polar caps: CO_2 clouds or low surface emissivity? J. Geophys. Res. 100, 21219–21234.

Forget, F., Hourdin, F., Talagrand, O., 1998. CO_2 snowfall on Mars: simulation with a General Circulation Model. Icarus 131, 302–316.

Forget, F., Hourdin, F., Fournier, R., Hourdin, C., Talagrand, O., Collins, M., Lewis, S.R., Read, P., Huot, J., 1999. Improved general circulation models of the martian atmosphere from the surface to above 80 km. J. Geophys. Res. 104, 24155–24176.

Georgelin, M., Lott, F., 2001. On the transfer of momentum by trapped lee waves: case of the IOP3 PYREX. J. Atmos. Sci. 58, 3563–3580.

Gierash, P.J., Goody, R.M., 1968. A study of the thermal and dynamical structure of the martian lower atmosphere. Planet. Space Sci. 16, 615–646.

Glandorf, D., Colaprete, A., Toon, O.B., Tolbert, M., Toon, O.B., 2002. CO_2 snow on Mars: experimental constraints. Icarus 160, 66–72.

Gooding, J.L., 1986. Martian dust particles as condensation nuclei—a preliminary assessment of mineralogical factors. Icarus 66, 56–74.

Hinson, D., 2001. Radio occultation measurements of forced atmospheric waves on Mars. J. Geophys. Res. 106, 1463–1480.

Hourdin, F., Armengaud, A., 1999. The use of finite-volume methods for atmospheric advection of trace species. Part I: Test of various formulations in a General Circulation Model. Mon. Weather Rev. 127, 822–837.

Hunt, G.E., Pickersgill, A.O., 1984. Some observations of martian cloud systems. Vistas Astron. 27, 131–148.

Ivanov, A.B., 2000. Some aspects of the martian climate in the Mars Orbiter Laser Altimeter (MOLA) investigation: Part II Polar night clouds. PhD thesis. Calif. Inst. of Technol., Pasadena.

Ivanov, A.B., Muhleman, D.O., 2001. Cloud reflection observations: results from the Mars Orbiter Laser Altimeter. Icarus 154, 190–206.

Jakosky, B.M., Martin, T.Z., 1987. Mars—north-polar atmospheric warming during dust storms. Icarus 72, 528–534.

James, P.B., Kieffer, H.H., Paige, D.A., 1992. The seasonal cycle of carbon dioxide on Mars. In: Kieffer, H.H., Jakosky, B.M., Snyder, C.W.,

Matthews, M.S. (Eds.), Mars. Univ. of Arizona Press, Tucson, pp. 934–968.

Kieffer, H.H., Martin, T.Z., Peterfreund, R., Jakosky, B.M., Miner, E.D., Palluconi, F.D., 1977. Thermal and albedo mapping during the Viking primary mission. J. Geophys. Res. 82, 4249–4291.

Lipps, F.B., Hemler, R.S., 1991. Numerical modeling of a midlatitude squall line: features of the convection and vertical momentum flux. J. Atmos. Sci. 48 (17), 1909–1929.

Lott, F., 1998. Linear mountain drag and averaged pseudo-momentum flux profiles in ther presence of trapped lee waves. Tellus 50A, 12–25.

MacKenzie, A.R., Haynes, P.H., 1992. The influence of surface kinetics on the growth of stratospheric ice crystals. J. Geophys. Res. 97, 8057–8064.

Ockert-Bell, M.B., Bell III, J.F., Pollack, J.B., McKay, C.P., Forget, F., 1997. Absorption and scattering properties of the martian dust in the solar wavelenghts. J. Geophys. Res. 102, 9039–9050.

Pearl, J.C., Smith, M.D., Conrath, B.J., Bandfield, J.L., Christensen, P.R., 2001. Observations of martian ice clouds by the Mars Global Surveyor Thermal Emission Spectrometer: the first martian year. J. Geophys. Res. 106, 12325–12338.

Pettengill, G.H., Ford, P.G., 2000. Winter clouds over the north martian polar cap. Geophys. Res. Lett. 27, 609–612.

Pickersgill, A.O., Hunt, G.E., 1979. The formation of martian lee waves generated by a crater. J. Geophys. Res. 84, 8317–8331.

Pirraglia, J.A., 1976. Martian atmospheric lee waves. Icarus 27, 517–530.

Pollack, G.H., Haberle, R.M., Schaeffer, J., Lee, H., 1990. Simulations of the general circulation of the martian atmosphere: 1. Polar processes. J. Geophys. Res. 95, 1447–1473.

Queney, P., 1947. Theory of perturbations in stratified currents with application to air flow over mountains, Misc23. The Univ. of Chicago Press.

Rossow, W.B., 1978. Cloud microphysics: analysis of the clouds of Earth, Venus, Mars, and Jupiter. Icarus 36, 1–50.

Scinocca, J.F., Shepherd, T.G., 1992. Nonlinear wave-activity conservation laws and Hamiltonian structure for the two-dimensional anelastic equations. J. Atmos. Sci. 49, 5–27.

Scorer, R., 1949. Theory of waves in the lee of mountains. Q. J. Roy Meteor. Soc. 75, 41–56.

Smith, R.B., 1980. Linear theory of stratified hydrostatic flow past an isolated mountain. J. Atmos. Sci. 32, 3483–3564.

Smith, D.E., Zuber, M.T., Frey, H.V., Garvin, J.B., Head, J.W., Muhleman, D.O., Pettengill, G.H., Phillips, R.J., Solomon, S.C., Zwally, H.J., Banerdt, W.B., Duxbury, T.C., Golombek, M.P., Lemoine, F.G., Neumann, G.A., et al., 2001a. Mars Orbiter Laser Altimeter: experiment summary after the first year of global mapping of Mars. J. Geophys. Res. 106, 23689–23722.

Smith, M.D., Pearl, J.C., Conrath, B.J., Christensen, P.R., 2001b. Thermal Emission Spectrometer results: Mars atmospheric thermal structure and aerosol distribution. J. Geophys. Res. 106, 23929–23945.

Wilson, R.J., 1997. A general circulation model of the martian polar warming. Geophys. Res. Lett. 24, 123–126.

Wood, S.E., 1999. Nucleation and growth of CO_2 ice crystals in the martian atmosphere. PhD thesis. Univ. of California, Los Angeles.

Yokohata, T., Odaka, M., Kuramoto, K., 2002. Role of H_2O and CO_2 ices in martian climate changes. Icarus 159, 439–448.

Zuber, M.T., Smith, D.E., Solomon, S.C., and colleagues, 1998. Observations of the north polar region from the Mars Orbiter Laser Altimeter. Science 279, 1686–1692.